PHYSICS

Observation of competing, correlated ground states in the flat band of rhombohedral graphite

Imre Hagymási[1,2,3,4]†, Mohammad Syahid Mohd Isa[5]†, Zoltán Tajkov[5,6], Krisztián Márity[5], László Oroszlány[7,8], János Koltai[6], Assem Alassaf[7], Péter Kun[5], Konrád Kandrai[5], András Pálinkás[5], Péter Vancsó[5], Levente Tapasztó[5], Péter Nemes-Incze[5]*

In crystalline solids, the interactions of charge and spin can result in a variety of emergent quantum ground states, especially in partially filled, topological flat bands such as Landau levels or in "magic angle" graphene layers. Much less explored is rhombohedral graphite (RG), perhaps the simplest and structurally most perfect condensed matter system to host a flat band protected by symmetry. By scanning tunneling microscopy, we map the flat band charge density of 8, 10, 14, and 17 layers and identify a domain structure emerging from a competition between a sublattice antiferromagnetic insulator and a gapless correlated paramagnet. Our density matrix renormalization group calculations explain the observed features and demonstrate that the correlations are fundamentally different from graphene-based magnetism identified until now, forming the ground state of a quantum magnet. Our work establishes RG as a platform to study many-body interactions beyond the mean-field approach, where quantum fluctuations and entanglement dominate.

INTRODUCTION

An important factor separating conventional and quantum magnets is that, in the latter, the mean-field description fails because of strong correlations and quantum fluctuations. Examples include antiferromagnetic spin chains (*1*) and ladders (*2*), where interactions result in exotic properties such as fractionalization and topological order (*3*). In general, condensed matter systems realizing quantum magnets have a complex structure, requiring the spins provided by the *d*-band of transition metals (*4*). On the other hand, graphene-based materials comprising only carbon atoms are simple and host a remarkable multitude of magnetic states, provided that a band with a divergent charge density is partially filled. This divergence can arise through a sublattice imbalance (*5*–*9*), through a Landau level (*10*, *11*), or in a moiré superlattice (*12*, *13*). Perhaps the simplest example of this is at the edges of zigzag nanoribbons, where, at charge neutrality (*14*), the spins on opposite sublattices interact antiferromagnetically (*5*). Further examples are in the layer antiferromagnet state of bilayer graphene (*9*, *15*, *16*) and in the sublattice-Néel state in trilayer (*17*–*19*) and tetralayer rhombohedral graphite (RG) (*20*–*22*), all explained within the mean-field approximation. This Néel state has the spins on opposing sublattices in an antiparallel configuration between the top and bottom surfaces and in a ferrimagnetic orientation within the same graphene layer. Mean-field Hubbard models predict it to be the gapped ground state at charge neutrality (*23*, *24*), measured in three- and four-layer RG by transport (*17*) and scanning tunneling microscopy (STM) (*22*). However, for thicker RG, interactions are expected to increase (*25*), holding the potential for driving a transition to a quantum magnet, providing a realization of graphene-based magnetism beyond the mean-field model.

Here, we show that, for thick RG, the gapped Néel state is not the ground state, because fluctuation terms and local correlations cannot be neglected. Instead, RG hosts domains of alternating gapped and gapless surface charge density, associated with a degenerate ground state. This degeneracy is a signature of quantum magnetism (*3*) that cannot be described at the mean-field level.

RG is distinct from any other graphene system in that it features a staggered intra- and interlayer hopping pattern (*26*), similar to a one-dimensional (1D) Su-Schrieffer-Heeger (SSH) model (*27*). It can be considered as built up from parallel SSH chains (Fig. 1A), leading to a sublattice imbalance on the top and bottom surfaces. A flat band is localized on the unpaired surface sublattice (blue in Fig. 1A) and decays into the bulk (*28*, *29*). The interacting 1D SSH chain (*30*, *31*) and "ladder materials" (*2*) with the chains linked up parallel to each other are elementary models for quantum magnets. This, together with recent evidence for strong correlations in thick samples (*32*), makes RG a prime candidate for quantum magnetism.

STM is a powerful tool to investigate correlated electron systems, for example, uncovering the inhomogeneities in the order parameter of high T_C superconductors (*33*) or nematicity in "magic angle" bilayer graphene (*34*–*37*). We present STM measurements at a temperature of 9.6 K, on the surface of SiO_2-supported RG (Fig. 1A). At half filling of the flat band (charge neutrality), two distinct phases of the surface state charge density appear: one having a splitting of up to 40 meV centered on the Fermi level, and the other being gapless. The two phases form a domain structure, characteristic of many-body competing ground states (*33*). Using density matrix renormalization group (DMRG) calculations, we identify that the surface hosts a net spin of $\mathcal{S} = 1$. This magnetic moment gives rise to a ground state of RG, which has degenerate spin projections on the surface of $s_z = \pm 1$ and $s_z = 0$. The $s_z = \pm 1$ surface state corresponds to the sublattice-Néel insulator, identified earlier using mean-field approaches: ab initio (*25*), Hubbard (*17*), Hartree-Fock (*38*), and continuum model (*39*) calculations. The $s_z = 0$ surface state is a correlated paramagnet, which is not present at the mean-field level

[1]Helmholtz-Zentrum Berlin für Materialien und Energie, 14109 Berlin, Germany. [2]Wigner Research Centre for Physics, 1121 Budapest, Hungary. [3]Dahlem Center for Complex Quantum Systems and Institut für Theoretische Physik, Freie Universität Berlin, 14195 Berlin, Germany. [4]Max Planck Institute for the Physics of Complex Systems, Dresden, Germany. [5]Centre for Energy Research, Institute of Technical Physics and Materials Science, 1121 Budapest, Hungary. [6]Department of Biological Physics, ELTE Eötvös Loránd University, 1117 Budapest, Hungary. [7]Department of Physics of Complex Systems, ELTE Eötvös Loránd University, 1117 Budapest, Hungary. [8]Budapest University of Technology and Economics, 1111 Budapest, Hungary.
*Corresponding author. Email: nemes.incze.peter@ek-cer.hu
†These authors contributed equally to this work.

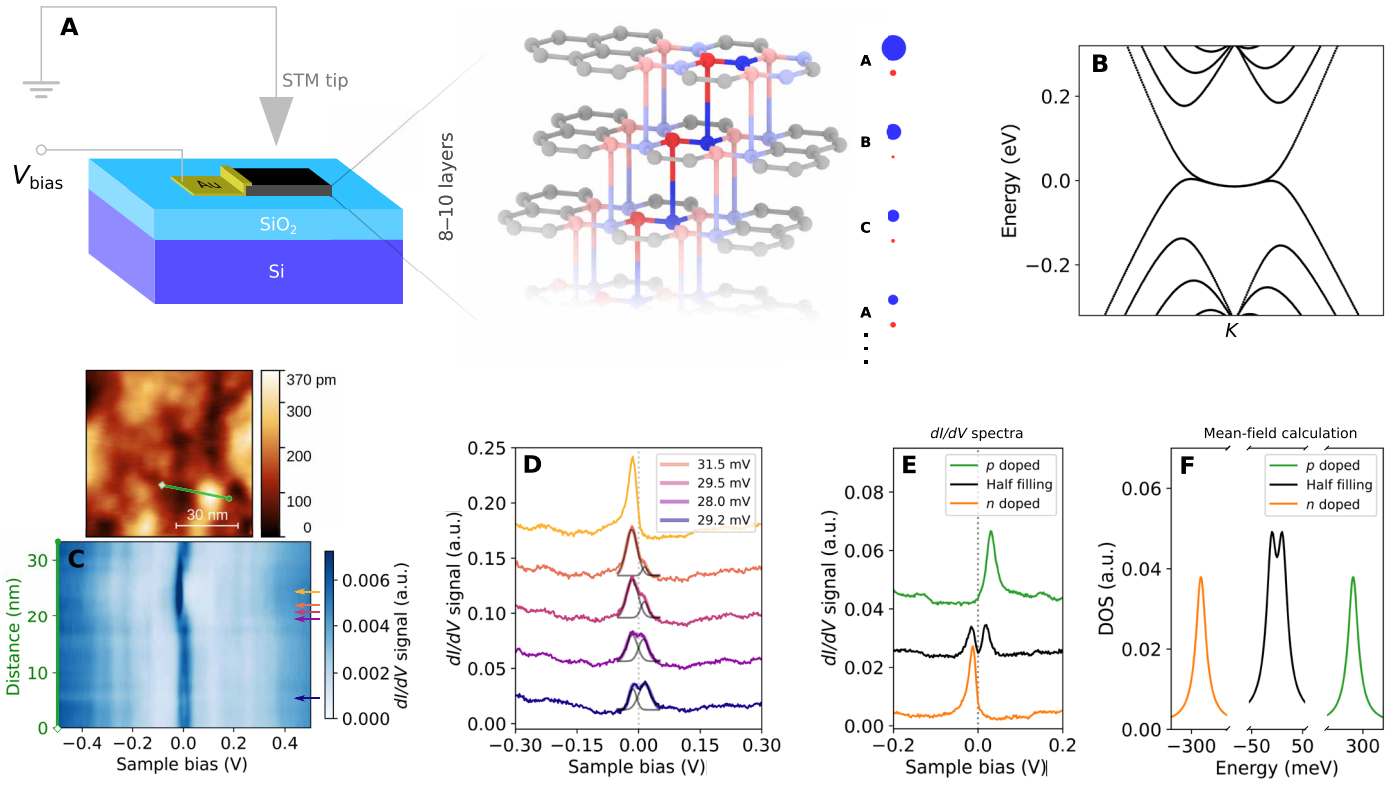

Fig. 1. Correlated insulating state in RG. (**A**) Schematic of the STM measurement setup, with the RG supported on a SiO_2 substrate. Blue and red atoms/bonds show the staggered, SSH-like (*27*) chain in RG (*26*). Nearest-neighbor chains, shown in light blue and red colors, form a ladder through interchain hoppings. The size of the blue and red circles next to the graphene layers is proportional to the large density of states (LDOS) on the respective sublattices. A, B, and C mark the characteristic stacking pattern of RG. (**B**) Calculated ab initio band structure of RG around the *K* point for eight layers. (**C**) Density plot of 64 *dI*/*dV* spectra measured along the green line shown in the STM topography image above (eight-layer sample). The surface state shifts in energy from being at the Fermi level to being almost completely filled and back to half filling. (**D**) Selected spectra, positions shown by arrows of the same color as in (C). The splitting in the surface state is always at the Fermi level, shown by the dotted line. Black Gaussians are fits to the surface state *dI*/*dV* peak, with a splitting shown in the inset. (**E**) *dI*/*dV* spectra measured in various positions on the sample surface, with the surface state below (orange), above (green), and at the Fermi level (black). The surface state shows a splitting of 32 meV at charge neutrality (black). The full width at half maximum (FWHM) of the completely filled or empty surface state is 26 meV. (**F**) Surface total DOS, calculated within the mean-field approach for various doping levels ($U = 6$ eV). Colors are with the same meaning as in (E). a.u., arbitrary units.

(*17*, *38*). The degeneracy between the gapless paramagnetic state and the antiferromagnetic insulator is an intrinsic property of RG and explains the domain structure of the surface state splitting observed experimentally.

RESULTS

Gapped and gapless domains at charge neutrality

We have used Raman spectroscopy to identify thick RG samples on a SiO_2 support (for details, see section S1.1) and performed STM measurements at multiple locations on an 8-, 10-, 14-, and 17-layer sample. The data presented in the main text are representative of the behavior seen in all samples. A topographic image of an 80-nm by 80-nm area of the eight-layer-thick sample is shown in Fig. 1C, while the large local density of states (LDOS) of the surface flat band shows up as a pronounced peak in the *dI*/*dV* spectra (Fig. 1, C to E). Alongside this peak, we can observe step-like features in the *dI*/*dV* signal starting below −150 mV and above +150 mV. These stem from dispersive, bulk bands visible in Fig. 1B, and their position in energy is a fingerprint of the number of layers in the RG sequence (see section S3). By tracking these peaks in the areas we investigate, we can ensure that the stacking sequence of RG is the same all over the measured surface (fig. S9D). The RG sample is only perturbed by the local charge and mechanical deformation inhomogeneity of the SiO_2 support. It is well known that this modulates the doping in the sample placed on top (*40*), and we use this inhomogeneity to our advantage. By simply moving the STM tip over the sample, we are able to investigate the surface state at various electron fillings.

Figure 1C shows spectra across a 35-nm-long line on the surface. The surface state suffers a local shift across the Fermi level (zero bias), with the selected spectra shown in Fig. 1D. We observe a ~30-meV splitting, centered on zero bias as soon as the surface state becomes partially filled with electrons, which is a strong indication of its many-body origin. In Fig. 1E, we highlight three representative cases, with the surface state at charge neutrality (black), filled (orange), and empty (green). In the latter two situations, the full width at half maximum (FWHM; *w*) is 26 meV, the narrowest peak width we measure. In this case, it is usually assumed that the effect of interactions is negligible. However, the filled and empty peaks show a shoulder on the right and left sides, respectively. This asymmetry is

characteristic of the doped spectra, similarly to the doped flat band peak of magic angle bilayers, indicating that e-e interactions are present, even near complete filling of the band (*34*, *37*). At half filling, the *dI*/*dV* peak shows a splitting of 32 meV. To reveal the origin of the observed peak splitting, we have performed calculations at the mean-field level, evidencing the opening of a gap due to antiferromagnetic exchange (see Fig. 1F and section S2 for details) (*17*). To rule out single-particle effects as the origin of the surface state splitting, we have modeled the effect of a perpendicular electric field and quantum confinement due to the electrostatic disorder potential of the sample. Using a density functional theory and a tight binding model, we found that these effects are not consistent with our observations either qualitatively or quantitatively. Splittings induced by quantum confinement are not pinned to the Fermi level and therefore are inconsistent with our observation. Furthermore, the perpendicular electric field needed to open a gap of 30 meV is orders of magnitude larger than what is present in our experiment. For a detailed discussion, see section S8.

Next, we have quantified the local variation of the splitting over large areas of the sample surface. By fitting two Gaussians to the surface state peak, we can extract the local splitting as the voltage difference between the peaks of the two Gaussians. The fitting was performed in the ±80-mV interval around zero bias. Examples of these fits can be seen in Figs. 1D and 2C. In Fig. 2A, we show a representative map of the local splitting in an 80-nm by 80-nm area. Details of the fitting procedure and more splitting maps are shown in sections S4 and S5.2. One notable feature of the map is that the sample contains regions with no observable splitting, although the flat band is half-filled in most of the area, as illustrated by spectrum #3, #II, and #IV in Fig. 2. The local charge density can be approximated by the spectral weight of the surface state below and above the Fermi level, similarly to the procedure used by Jiang *et al.* (*35*) in the case of magic angle bilayer graphene. After subtracting the background from the *dI*/*dV* spectra, we measure the area of the peak under the Fermi level (A_{under}) up to the peak edge (−100 mV). Examples of this can be seen in Fig. 2F. We define the fill ratio as $A_{\text{under}}/A_{\text{total}}$, where A_{total} is the total area under the peak. We consider half filling or charge neutrality to be at 50% fill ratio. The local charge density measured this way is also correlated with the shift in bias voltage of the bulk bands (for more details, see section S5.1).

A map of the local fill ratio (Fig. 2E) shows that, in most areas, the peak is between 30 and 60% filled. There are substantial areas of near half filling in both domains with large splitting and no splitting at all. This is unexpected at first because the mean-field ground state in tri- and tetralayers is gapped (*17*, *20*, *22*). The presence of a gapless surface density indicates the failure of the mean-field approximation to fully capture the behavior of eight-layer RG. The domain structure is also apparent if we fit a single Gaussian to the spectra and plot the FWHM *w*, which shows a bimodal distribution

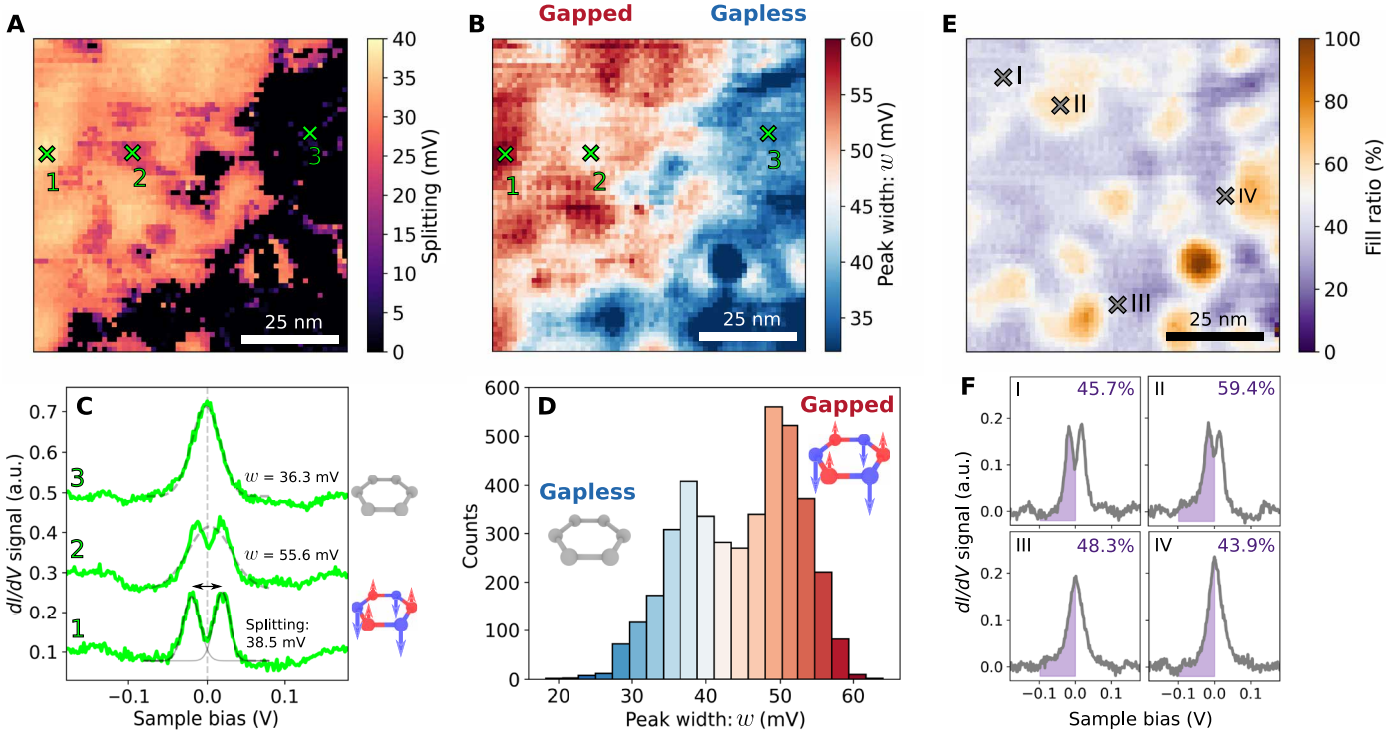

Fig. 2. Gapped and gapless domains. (**A**) Map of the surface state splitting over an 80-nm by 80-nm area of the sample, measured using a grid of 64 × 64 *dI*/*dV* spectra. STM topographic image of the region can be seen in Fig. 1C. The splitting was determined by fitting two Gaussians to the peak. Examples of fits can be seen in (C) and Fig. 1D. (**B**) FWHM (*w*) of the peak from the same *dI*/*dV* map, obtained by fitting a single Gaussian (for fitting details, see section S4). (**C**) Examples of individual *dI*/*dV* spectra measured in locations shown by numbers on (A) and (B). Double- and single-Gaussian fits are shown by gray dashed curved lines, and the splitting and ω values are shown next to the spectra. (**D**) Histogram of peak widths (ω) in the data of (B). (**E**) Map of the local fill ratio as defined in the main text for the area shown in (A). (**F**) Selected spectra measured at the positions marked by crosses and roman numerals in (E). Purple shading shows the area under the peak used to determine the fill ratios shown in the inset in %. Tip stabilization parameters are as follows: 100 pA and 500 mV.

(Fig. 2D). Furthermore, the peak width in the areas without splitting is at least 10 mV larger than in the fully doped case, suggesting that many-body effects do play a role in this case. We call the areas without splitting as gapless, up to the energy resolution of our measurement, meaning that we cannot rule out the presence of a gap smaller than 4.5 meV. In the measurements, a slight deviation from charge neutrality, but with the Fermi level still near half filling, does not alter the gapped or gapless nature of the peak, as can be seen in Figs. 1D and 2.

Degenerate ground state in RG and the breakdown of the mean-field approximation

The dual nature of the flat band charge density is remarkable, because at the mean-field level, gapless ground states are not expected to be stable (*38*). The DMRG approach goes beyond the mean-field approximation and allows us to compute the complete many-body wave function, taking quantum fluctuations fully into account that are crucial in low-dimensional systems. Figure 3A shows the magnetic moments on the top four graphene layers along a staggered chain of RG, calculated using DMRG. The local moments show a ferrimagnetic ordering on the graphene sublattices, which decay into the bulk to near zero by the third graphene layer. It can be seen that the mean-field calculations also reproduce this sublattice-Néel magnetic ordering, where the total spin for one surface, s_z, within the RG unit cell is 1. In our mean-field calculations, this Néel ordering forms an insulating state (*23*, *24*), with a splitting shown in Fig. 1F. The splitting observed in the *dI*/*dV* maps is a signature of this insulating state. One expects an insulator because the magnetic ordering breaks the inversion and time reversal symmetries protecting the gapless state at charge neutrality (*41*).

Beyond the agreement on the magnetic ordering, we find that the mean-field approach overestimates the ground-state energy of RG by 5.16 meV per atom compared to the DMRG result, highlighting the importance of correlation effects in the system (for more details, see section S2). In DMRG calculations, the ground state of the RG slab features spins localized to the bottom and top layers, with a total spin of $\mathcal{S}_T$ and a spin projection of $\mathcal{S}_{T,z}$. In Fig. 3B, we plot the ground-state energies as a function of the two-site approximation of the full variance v, defined by $v = \langle H^2 \rangle - \langle H \rangle^2$, where H denotes the Hamiltonian and $\langle \ldots \rangle$ denotes the expectation value with respect to the variational state. Three different configurations of the total spin, $\mathcal{S}_T = 0,1,2$, converge to the exact ground state at $v = 0$, all of them being degenerate. Because in STM we are probing only one surface, these total spin states correspond to three possible spin projections on the top surface: $s_z = 0, \pm 1$. Among these, the $s_z = \pm 1$ (Néel) also features the mean-field result, with the +1 state

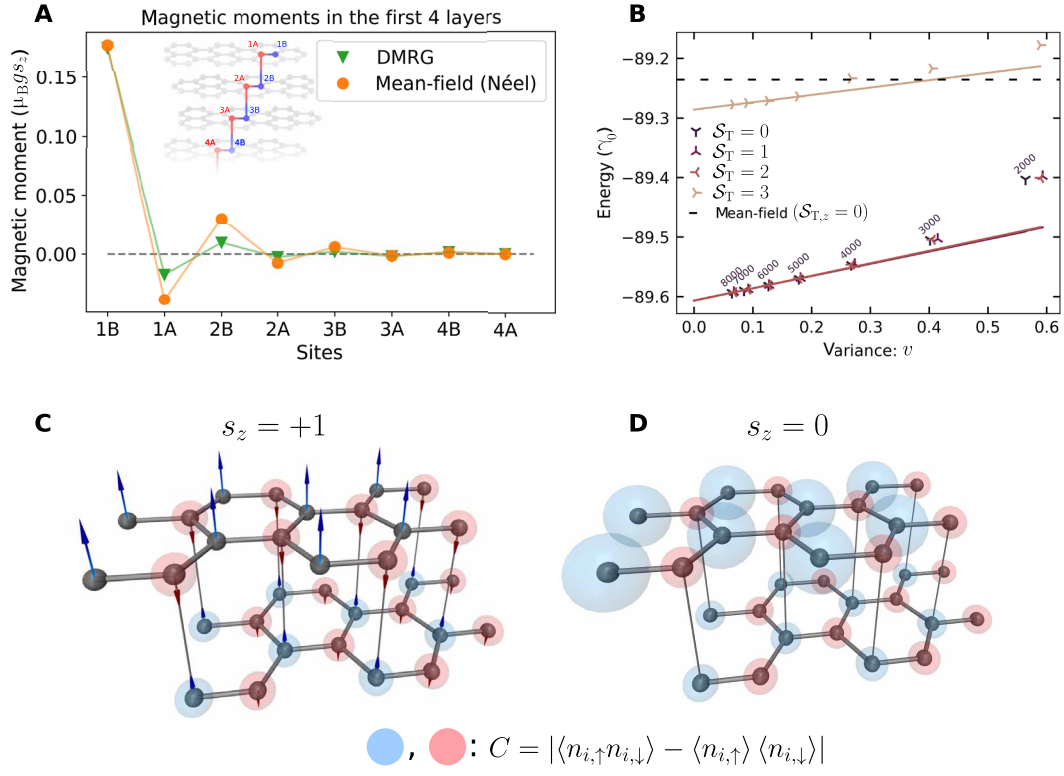

Fig. 3. DMRG and mean-field Hubbard model calculations. (**A**) Calculated local magnetic momenta for a six-layer RG. The magnetic moments on the atomic sites decay exponentially, essentially to zero after the second graphene layer ($U = 0.5 \times \gamma_0$). Inset shows one staggered chain of RG in red and blue atoms, along which the plot is performed. (**B**) DMRG calculations of the ground states of a six-layer-thick cell as a function of the variance. Energy in units of the nearest-neighbor hopping term: γ_0. The exact ground state is reached at zero variance. The states with various total spin of whole cell (both top and bottom graphene layers): $\mathcal{S}_T$ are degenerate, with a ground state that is 5.16 meV per atom smaller than the mean-field case (dashed line). The first excited spin state ($\mathcal{S}_T = 3$) is $0.33 \times \gamma_0$. (**C** and **D**) Colored arrows showing the distribution of magnetic moments on the top two graphene layers with a surface spin of s_z, from the DMRG calculation. The magnetic moments μ are scaled by $2\,|\mu|^{1/4}$ for better visibility. The radius of the opaque spheres is proportional to the local electronic correlation C values, as defined by the relation shown. $\langle n_{i,\uparrow} \rangle$ and $\langle n_{i,\downarrow} \rangle$ are the expectation values of the spin density on the atomic site i. Blue and red colors distinguish the two graphene sublattices.

shown in Fig. 3C and the −1 state corresponding to the case, where the spins are inverted. These two states are indistinguishable if the STM tunneling current is not spin polarized. However, the $s_z = 0$ instance has no analog in the mean-field approximation, because the mean-field decoupling excludes the possibility to host a correlated state and only magnetic solutions can result in a lower energy. This correlation effect is shown in Fig. 3 (C and D), where the radius of the colored spheres is proportional to the calculated charge correlation values (C). Instead of the magnetic moments, the $s_z = 0$ solution shows an enhanced local charge correlation on the unpaired sublattice, forming a correlated paramagnet on the surface. In this state, the charge fluctuations are more and more suppressed with increasing U (the electrons prefer not to hop to already occupied sites), and the total energy is decreased directly by the smaller number of doubly occupied sites instead of long-range magnetic ordering. This is a truly many-body effect, because the mean-field approach is only able to decrease the total energy via magnetic ordering and not by decreasing the doubly occupied sites. This state is gapless for the charge degree of freedom, because there is no large-scale breaking of symmetries (*41*), as opposed to the $s_z = \pm 1$ case. The two degenerate states form a natural candidate for the domain structure observed in STM, with a gapped antiferromagnetic insulator and a gapless, correlated paramagnet. Globally, over the whole sample surface, none of the two states can dominate, but locally because of inhomogeneities, the system can favor either the $s_z = \pm 1$ or the $s_z = 0$ state, similarly to competing states in strongly correlated materials (*33*).

Last, we have calculated the energy of the $\mathcal{S}_T = 3$ state and find that it is $0.33 \times \gamma_0$ higher than the ground state for a six-layer-thick cell (Fig. 3B), with γ_0 being the nearest-neighbor hopping of graphene. This gap separates the first (bulk) excited spin state of RG from the degenerate ground state. The large size (~1 eV) of the spin gap is responsible for the rapid decay of the magnetic moments (s_z) at the top and bottom graphene layers.

Critical temperature

Having established the presence of correlated insulating and gapless phases, we have checked their temperature dependence. In Fig. 4 (A and B), we show another example of the domain structure of the surface state splitting. By measuring the same 80-nm by 80-nm area of the sample at increasing temperature, we observe that the splitting and w suddenly decrease at a temperature of 17 K all across the surface.

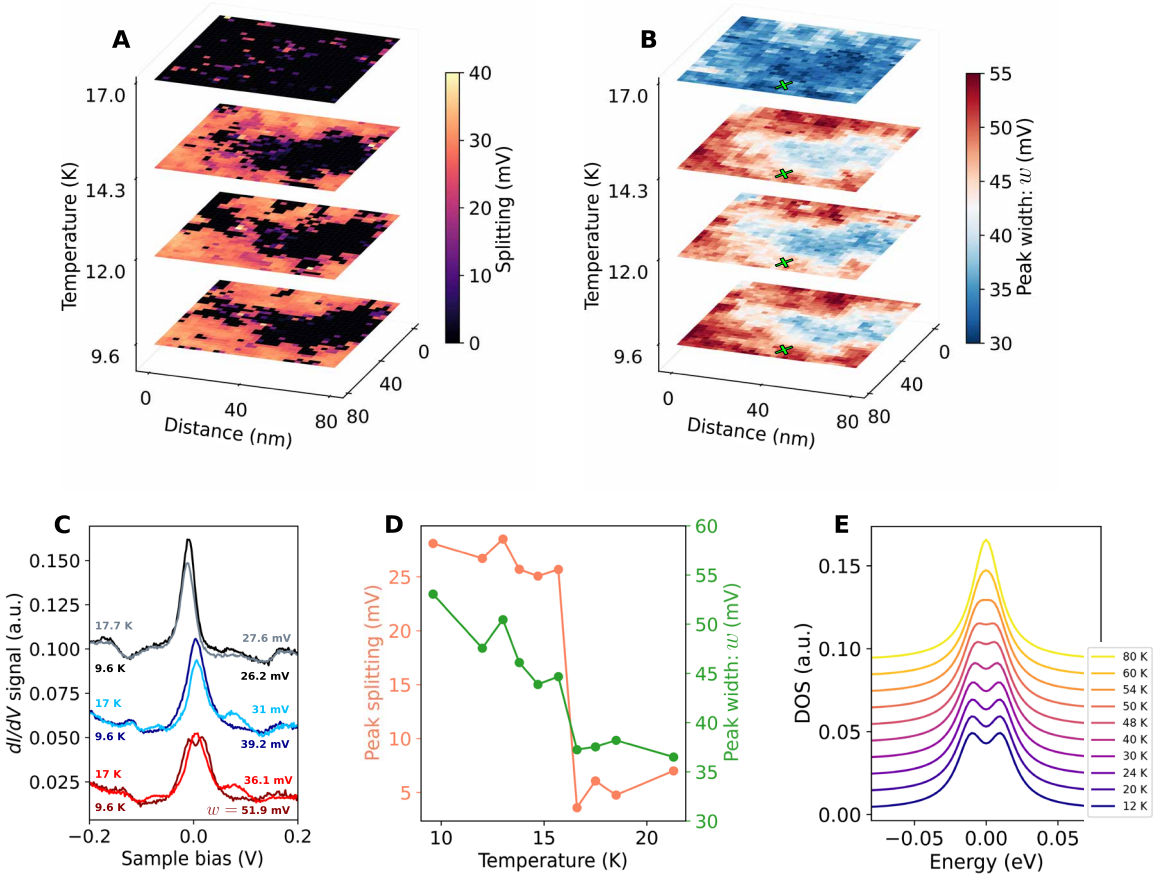

Fig. 4. Temperature dependence. (**A**) Map of the surface state splitting in an 80-nm by 80-nm area on the eight-layer sample. The same area is measured at four different temperatures. (**B**) Map of ω in the same area and temperatures as in (A). Above 16.6 K, the splitting vanishes and the peak width decreases sharply. (**C**) Selected spectra in a gapped (bottom), gapless (middle), and completely filled (top) area below and above the critical temperature. The width w of the peaks are shown in millivolts next to the spectra. Spectra at different temperatures are measured in the same location. (**D**) Peak splitting (orange) and ω of the surface state (green) as a function of temperature, measured in the position marked by the green crosses in (B). Connecting lines are guide to the eye. (**E**) Temperature-dependent mean-field calculation of the splitting at charge neutrality ($U = 6$ eV).

Example spectra are shown in Fig. 4C in a gapped (red) and a gapless (blue) region, measured at different temperatures in the same surface position. Raising the temperature from 9.6 to 17 K, the surface state becomes a single peak with decreasing w. This is in contrast to a highly doped area (gray spectra), where w increases by 1.4 mV, corresponding to the extra broadening due to the increased temperature (see also fig. S13).

This suggests the presence of a phase transition at charge neutrality. We identify as the critical temperature the value where the splitting collapses and the width of the peak stops decreasing and plateaus. Values measured on different areas of the sample show a variation. The value of T_C for the area shown in Fig. 4 is 16.6 K, with the highest T_C measured to be 22 K (see section S6). Above T_C, the dI/dV peak width is still roughly 10 meV wider than the w expected from a single-particle band structure (26 meV), suggesting that some many-body effects might still play a role at these temperatures. Our temperature-dependent mean-field calculation reproduces the narrowing of the peak by increasing temperature, but as expected, it overestimates T_C (Fig. 4E).

Having determined the splitting and bandwidth in our sample, it is instructive to compare it to STM measurements of a four-layer RG sample and to the correlated insulator states observed in magic angle twisted bilayer graphene. In the former case, measurements by Kerelsky *et al.* (*22*) show a FWHM of the surface state peak between 3 and 5 meV, while the splitting is 9.5 meV at half filling. In our measurement of the eight-layer RG, the FWHM is 25 meV, with a splitting in the 30- to 40-meV range. Thus, the rearrangement of the spectral weight (splitting) due to interactions exceeds the bandwidth (FWHM) of the peak, which is a clear sign of strong correlations. By this measure, the eight-layer RG is also comparable to magic angle bilayers, where the splitting between the two flat band dI/dV peaks increases by 15 to 20 meV near charge neutrality, also exceeding the bandwidth of around 10 meV (*34*, *37*).

Measurements of the surface state charge density in a 14-layer RG sample were also carried out by Henck *et al.* (*42*) using nano–angle-resolved photoemission spectroscopy measurements. Below the Fermi level, they measure a FWHM of the surface state of 50 meV at a temperature of 90 K. In their discussion, the authors assume that the sample is charge neutral, with a surface state splitting of 40 meV, surviving up to the measurement temperature. The value of the splitting is comparable to our measurements, but their assumption that the critical temperature is higher than 90 K is not consistent with our STM data.

Possible symmetry breaking away from charge neutrality

We now turn our attention to the situation when the surface state is away from charge neutrality but not completely filled/empty. In general, strongly interacting materials display a whole range of different ground states as function of charge carrier density (*33*). Three-layer RG is no exception; both ferromagnetism (*43*) and superconductivity (*44*) appear at various doping intervals. It is only natural to assume that thicker RG samples should host similarly rich many-body phases.

Our mean-field calculations at slight doping (2.16×10^{12} cm^{-2}; Fig. 5B) suggest that the gap closes, but the surface magnetization does not vanish. Instead, it forms a ferromagnetic pattern with a $(\sqrt{3} \times \sqrt{3})R30^\circ$ enlarged unit cell (Fig. 5C). At this doping, mean-field calculations suffice because we are dealing with a magnetic state. Nevertheless, we have checked that DMRG calculations also reproduce this enlarged unit cell, and the magnetizations agree well with the mean-field ones. This translation symmetry breaking is also present in the total LDOS, which is the quantity that is measured by STM.

We have been able to identify an area of the sample with slight p doping, as evidenced by the spectrum shown in Fig. 5A. Measuring the dI/dV signal inside the surface state at 20-mV bias voltage shows a $\sqrt{3} \times \sqrt{3}$ modulation that enlarges the unit cell, both in the graphite lattice and in the Fourier transform of the data (Fig. 5D). The presence of this superlattice is not evidence in itself for the predicted ferromagnetic pattern, because these patterns can be also created by intervalley scattering due to lattice defects, such as vacancies. To rule out these surface defects as the origin of the pattern, we show in fig. S14 a 12-nm by 12-nm topographic image showing that vacancies are not present on the top graphene layer around the area of interest. Furthermore, strong lattice defects cause intervalley scattering of all states regardless of energy, albeit with decreasing amplitude (*45*). In our case, measuring at a 100-mV bias voltage outside the surface state in the same area of the sample simply shows the expected periodicity of graphite (Fig. 5E). This is an unusual behavior for a defect-induced LDOS modulation, providing a possible signature for the predicted ferromagnetic state. However, subsurface defects can also lead to a slight modulation of the LDOS in the top graphene layer (*46*), and the behavior of these is less well studied. Therefore, we cannot completely rule out the defect origin of the $\sqrt{3}$ modulation we observe.

Ferromagnetism has been predicted at finite doping (*47*) and has been recently measured in the compressibility of trilayer RG (*43*). Our calculations suggest that ferromagnetism is also present in thick RG and is accompanied by translation symmetry breaking. At present, it is still unclear whether the interaction-induced $\sqrt{3} \times \sqrt{3}$ instability is accompanied by the formation of a Kekulé gap (*48*–*50*) or some other valley order (*39*, *51*).

DISCUSSION

We have shown that interactions in the surface state of thick RG produce a ground state that is fundamentally different from the mean-field prediction, having a domain structure of gapped and gapless surface charge density. According to our DMRG calculations, this domain structure is a result of the degenerate ground state. The fundamental difference between three to four layers and thick samples is that, in the latter, the surface states on opposite graphene terminations do not overlap (*32*). Such an overlap changes the nature of the quantum magnet and lifts the characteristic degeneracy, resulting in a completely gapped ground state, as recently shown in spin chains of triangulene (*7*). As a consequence, the surface charge density in tetralayers is always gapped and magnetic; therefore, it is well described by mean-field theory (*22*). Perhaps most importantly, RG provides a platform for the straightforward tuning of the correlated phase discussed here, through electric and magnetic fields (*32*) and by mechanical strain, in a simple defect-free quantum material.

Although we do not directly measure the sample magnetization, charge transport measurements of Shi *et al.* (*32*) show hysteretic behavior of the resistance in a magnetic field, supporting the notion that thick RG hosts a nonzero magnetic moment. Their measurements also hinted at the formation of insulating domains, which our STM measurements confirm. Because the interacting surface

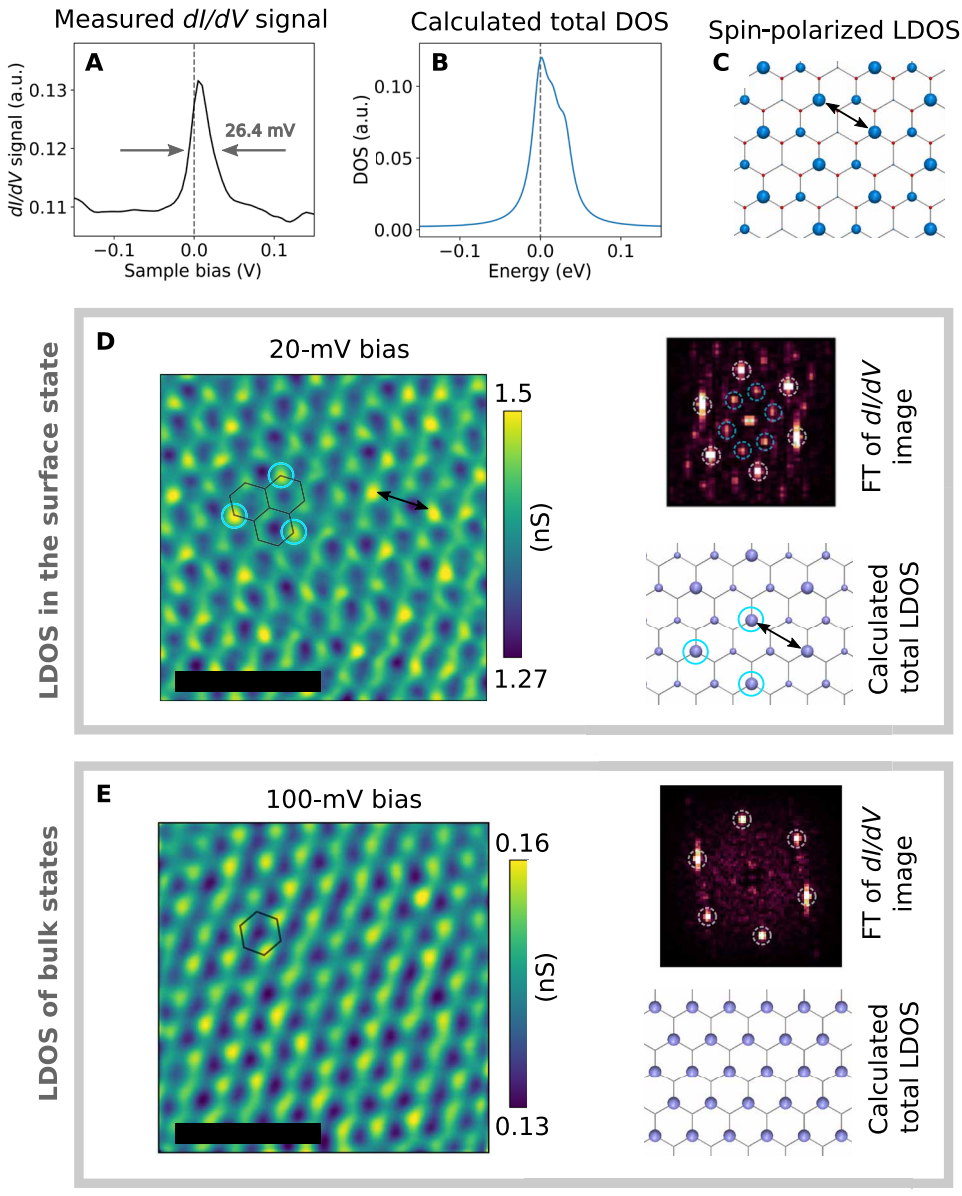

Fig. 5. Possible ferromagnetism and spontaneous breaking of translational symmetry. (**A**) *dI/dV* spectrum measured in an area with slight *p* doping. FWHM (*w*) of the surface state peak is 26.4 mV. (**B**) DOS for *p* doping of 2.16×10^{12} cm^{-2}, similar to the experiment, calculated by the mean-field model. (**C**) Mean-field calculation of the spin-resolved LDOS of the top layer of *p*-doped RG. Size of circles is proportional to the LDOS of the top graphene layer in the flat band ($U = 4.2$ eV). The LDOS shows essentially a ferromagnet. Blue, up spin; red, down spin. The black arrow marks the $\sqrt{3}\times$ enlarged unit cell size. This magnetization pattern is also reproduced in DMRG. (**D**) STM of the *dI/dV* signal inside the surface state. The black arrows and light blue circles show the enlarged unit cell size. Stabilization parameters are as follows: 30 pA and 20 mV. (**E**) *dI/dV* image far from the surface state, measured in the same area as (D). Stabilization parameters are as follows: 70 pA and 100 mV. Insets in (D) and (E): Fourier transform of the *dI/dV* image. White, dashed circles show the atomic periodicity corresponding to the 2.46-Å˚ unit cell of graphene. Light blue, dashed circles show the unit cell of $2.46 \times \sqrt{3}$ Å. The size of the blue spheres is proportional to the calculated total LDOS in the flat band (D) and 240 meV above the flat band (E). Scale bars, 1 nm in length (*dI/dV* images). Stabilization parameters in (D) and (E) are chosen, such that the tip-sample distance stays the same. Measurement temperature, 9.6 K; bias modulation, 20 mV. FT, Fourier transform.

state is easily accessible, future studies by spin-polarized STM would be especially fruitful in directly identifying the surface magnetic moments.

Our DMRG calculations show that, at charge neutrality, the spin and charge interactions in RG result in a degenerate ground state and a bulk spin gap. These properties are also shared by a simpler toy model, the 1D quantum spin chain with a bulk spin of 2 (*1*, *52*), raising the following question: What other properties of this famous toy model are shared by RG? Further theoretical and experimental investigations exploring the properties of this new system hold the promise of revealing the existence of nonlocal topological order, spin or charge fractionalization (*7*, *52*, *53*), and perhaps unconventional superconductivity (*44*, *54*).

MATERIALS AND METHODS

Samples of RG were exfoliated onto Si/SiO_2 surfaces from natural graphite crystals ("graphenium"), purchased from NGS Trading & Consulting GmbH. RG crystals were identified by Raman spectroscopy, with a laser excitation of 532 nm. Before STM measurements, Ti/Au electrodes were evaporated onto the samples using a stencil mask. STM measurements were conducted in a commercial ultrahigh vacuum (UHV) STM (RHK Freedom), at a temperature of 9.6 K and a base pressure of 5×10^{-11} torr. For variable temperature measurements, a resistive heater was used with a closed-loop temperature controller. Mechanically cut Pt/Ir tips were calibrated on a Au (111) surface before measurement.

SUPPLEMENTARY MATERIALS

Supplementary material for this article is available at https://science.org/doi/10.1126/sciadv.abo6879

REFERENCES AND NOTES

1. F. D. M. Haldane, Nonlinear field theory of large-spin Heisenberg antiferromagnets: Semiclassically quantized solitons of the one-dimensional easy-axis Néel state. *Phys. Rev. Lett.* **50**, 1153–1156 (1983).
2. E. Dagotto, T. M. Rice, Surprises on the way from one- to two-dimensional quantum magnets: The ladder materials. *Science* **271**, 618–623 (1996).
3. U. Schollwöck, J. Richter, D. J. J. Farnell, R. F. Bishop, *Quantum Magnetism* (Springer, 2004).
4. A. Vasiliev, O. Volkova, E. Zvereva, M. Markina, Milestones of low-d quantum magnetism. *NPJ Quant. Mater.* **3**, 18 (2018).
5. G. Z. Magda, X. Jin, I. Hagymási, P. Vancsó, Z. Osváth, P. Nemes-Incze, C. Hwang, L. P. Biró, L. Tapasztó, Room-temperature magnetic order on zigzag edges of narrow graphene nanoribbons. *Nature* **514**, 608–611 (2014).
6. S. Just, S. Zimmermann, V. Kataev, B. Büchner, M. Pratzer, M. Morgenstern, Preferential antiferromagnetic coupling of vacancies in graphene on SiO_2: Electron spin resonance and scanning tunneling spectroscopy. *Phys. Rev. B* **90**, 125449 (2014).
7. S. Mishra, G. Catarina, F. Wu, R. Ortiz, D. Jacob, K. Eimre, J. Ma, C. A. Pignedoli, X. Feng, P. Ruffieux, J. Fernández-Rossier, R. Fasel, Observation of fractional edge excitations in nanographene spin chains. *Nature* **598**, 287–292 (2021).
8. Y. Lemonik, I. Aleiner, V. I. Fal'ko, Competing nematic, antiferromagnetic, and spin-flux orders in the ground state of bilayer graphene. *Phys. Rev. B* **85**, 245451 (2012).
9. T. C. Lang, Z. Y. Meng, M. M. Scherer, S. Uebelacker, F. F. Assaad, A. Muramatsu, C. Honerkamp, S. Wessel, Antiferromagnetism in the hubbard model on the bernal-stacked honeycomb bilayer. *Phys. Rev. Lett.* **109**, 126402 (2012).
10. A. F. Young, C. R. Dean, L. Wang, H. Ren, P. Cadden-Zimansky, K. Watanabe, T. Taniguchi, J. Hone, K. L. Shepard, P. Kim, Spin and valley quantum hall ferromagnetism in graphene. *Nat. Phys.* **8**, 550–556 (2012).
11. A. F. Young, J. D. Sanchez-Yamagishi, B. Hunt, S. H. Choi, K. Watanabe, T. Taniguchi, R. C. Ashoori, P. Jarillo-Herrero, Tunable symmetry breaking and helical edge transport in a graphene quantum spin hall state. *Nature* **505**, 528–532 (2014).
12. A. L. Sharpe, E. J. Fox, A. W. Barnard, J. Finney, K. Watanabe, T. Taniguchi, M. A. Kastner, D. Goldhaber-Gordon, Emergent ferromagnetism near three-quarters filling in twisted bilayer graphene. *Science* **365**, 605–608 (2019).
13. G. Chen, A. L. Sharpe, E. J. Fox, Y.-H. Zhang, S. Wang, L. Jiang, B. Lyu, H. Li, K. Watanabe, T. Taniguchi, Z. Shi, T. Senthil, D. Goldhaber-Gordon, Y. Zhang, F. Wang, Tunable correlated chern insulator and ferromagnetism in a moiré superlattice. *Nature* **579**, 56–61 (2020).
14. P. Vancsó, I. Hagymási, L. Tapasztó, A magnetic phase-transition graphene transistor with tunable spin polarization. *2D Mater.* **4**, 024008 (2017).
15. J. Velasco, L. Jing, W. Bao, Y. Lee, P. Kratz, V. Aji, M. Bockrath, C. N. Lau, C. Varma, R. Stillwell, D. Smirnov, F. Zhang, J. Jung, A. H. MacDonald, Transport spectroscopy of symmetry-broken insulating states in bilayer graphene. *Nat. Nanotechnol.* **7**, 156–160 (2012).
16. F. R. Geisenhof, F. Winterer, A. M. Seiler, J. Lenz, T. Xu, F. Zhang, R. T. Weitz, Quantum anomalous hall octet driven by orbital magnetism in bilayer graphene. *Nature* **598**, 53–58 (2021).
17. Y. Lee, D. Tran, K. Myhro, J. Velasco, N. Gillgren, C. N. Lau, Y. Barlas, J. M. Poumirol, D. Smirnov, F. Guinea, Competition between spontaneous symmetry breaking and single-particle gaps in trilayer graphene. *Nat. Commun.* **5**, 5656 (2014).
18. M. Yankowitz, J. I.-J. Wang, A. G. Birdwell, Y.-A. Chen, K. Watanabe, T. Taniguchi, P. Jacquod, P. San-Jose, P. Jarillo-Herrero, B. J. LeRoy, Electric field control of soliton motion and stacking in trilayer graphene. *Nat. Mater.* **13**, 786–789 (2014).
19. S. Hattendorf, A. Georgi, M. Liebmann, M. Morgenstern, Networks of ABA and ABC stacked graphene on mica observed by scanning tunneling microscopy. *Surf. Sci.* **610**, 53–58 (2013).
20. K. Myhro, S. Che, Y. Shi, Y. Lee, K. Thilahar, K. Bleich, D. Smirnov, C. N. Lau, Large tunable intrinsic gap in rhombohedral-stacked tetralayer graphene at half filling. *2D Mater.* **5**, 045013 (2018).
21. Y. Lee, S. Che, J. Velasco Jr., D. Tran, J. Baima, F. Mauri, M. Calandra, M. Bockrath, C. N. Lau, Gate tunable magnetism and giant magnetoresistance in ABC-stacked few-layer graphene. arXiv:1911.04450 [cond-mat.mes-hall] (11 November 2019).
22. A. Kerelsky, C. Rubio-Verdú, L. Xian, D. M. Kennes, D. Halbertal, N. Finney, L. Song, S. Turkel, L. Wang, K. Watanabe, T. Taniguchi, J. Hone, C. Dean, D. N. Basov, A. Rubio, A. N. Pasupathy, Moiréless correlations in ABCA graphene. *Proc. Natl. Acad. Sci. U.S.A.* **118**, e2017366118 (2021).
23. D.-H. Xu, J. Yuan, Z.-J. Yao, Y. Zhou, J.-H. Gao, F.-C. Zhang, Stacking order, interaction, and weak surface magnetism in layered graphene sheets. *Phys. Rev. B* **86**, 201404 (2012).
24. J. H. Muten, A. J. Copeland, E. McCann, Exchange interaction, disorder, and stacking faults in rhombohedral graphene multilayers. *Phys. Rev. B* **104**, 035404 (2021).
25. B. Pamuk, J. Baima, F. Mauri, M. Calandra, Magnetic gap opening in rhombohedral-stacked multilayer graphene from first principles. *Phys. Rev. B* **95**, 075422 (2017).
26. H. Min, A. H. MacDonald, Electronic structure of multilayer graphene. *Progr. Theoret. Phys. Suppl.* **176**, 227–252 (2008).
27. W. P. Su, J. R. Schrieffer, A. J. Heeger, Solitons in polyacetylene. *Phys. Rev. Lett.* **42**, 1698–1701 (1979).
28. R. Xiao, F. Tasnádi, K. Koepernik, J. W. F. Venderbos, M. Richter, M. Taut, Density functional investigation of rhombohedral stacks of graphene: Topological surface states, nonlinear dielectric response, and bulk limit. *Phys. Rev. B* **84**, 165404 (2011).
29. S. Slizovskiy, E. McCann, M. Koshino, V. I. Fal'ko, Films of rhombohedral graphite as two-dimensional topological semimetals. *Commun. Phys.* **2**, 164 (2019).
30. K. Nawa, K. Tanaka, N. Kurita, T. J. Sato, H. Sugiyama, H. Uekusa, S. Ohira-Kawamura, K. Nakajima, H. Tanaka, Triplon band splitting and topologically protected edge states in the dimerized antiferromagnet. *Nat. Commun.* **10**, 2096 (2019).
31. N. H. Le, A. J. Fisher, N. J. Curson, E. Ginossar, Topological phases of a dimerized Fermi–Hubbard model for semiconductor nano-lattices. *NPJ Quant. Inform.* **6**, 24 (2020).
32. Y. Shi, S. Xu, Y. Yang, S. Slizovskiy, S. V. Morozov, S.-K. Son, S. Ozdemir, C. Mullan, J. Barrier, J. Yin, A. I. Berdyugin, B. A. Piot, T. Taniguchi, K. Watanabe, V. I. Fal'ko, K. S. Novoselov, A. K. Geim, A. Mishchenko, Electronic phase separation in multilayer rhombohedral graphite. *Nature* **584**, 210–214 (2020).
33. E. Dagotto, Complexity in strongly correlated electronic systems. *Science* **309**, 257–262 (2005).
34. A. Kerelsky, L. J. McGilly, D. M. Kennes, L. Xian, M. Yankowitz, S. Chen, K. Watanabe, T. Taniguchi, J. Hone, C. Dean, A. Rubio, A. N. Pasupathy, Maximized electron interactions at the magic angle in twisted bilayer graphene. *Nature* **572**, 95–100 (2019).
35. Y. Jiang, X. Lai, K. Watanabe, T. Taniguchi, K. Haule, J. Mao, E. Y. Andrei, Charge order and broken rotational symmetry in magic-angle twisted bilayer graphene. *Nature* **573**, 91–95 (2019).
36. Y. Choi, J. Kemmer, Y. Peng, A. Thomson, H. Arora, R. Polski, Y. Zhang, H. Ren, J. Alicea, G. Refael, F. von Oppen, K. Watanabe, T. Taniguchi, S. Nadj-Perge, Electronic correlations in twisted bilayer graphene near the magic angle. *Nat. Phys.* **15**, 1174–1180 (2019).
37. Y. Xie, B. Lian, B. Jäck, X. Liu, C.-L. Chiu, K. Watanabe, T. Taniguchi, B. A. Bernevig, A. Yazdani, Spectroscopic signatures of many-body correlations in magic-angle twisted bilayer graphene. *Nature* **572**, 101–105 (2019).
38. J. Jung, A. H. MacDonald, Gapped broken symmetry states in ABC-stacked trilayer graphene. *Phys. Rev. B* **88**, 075408 (2013).
39. F. Zhang, J. Jung, G. A. Fiete, Q. Niu, A. H. MacDonald, Spontaneous quantum hall states in chirally stacked few-layer graphene systems. *Phys. Rev. Lett.* **106**, 156801 (2011).
40. Y. Zhang, V. W. Brar, C. Girit, A. Zettl, M. F. Crommie, Origin of spatial charge inhomogeneity in graphene. *Nat. Phys.* **5**, 722–726 (2009).
41. J. L. Mañes, F. Guinea, M. A. H. Vozmediano, Existence and topological stability of fermi points in multilayered graphene. *Phys. Rev. B* **75**, 155424 (2007).
42. H. Henck, J. Avila, Z. Ben Aziza, D. Pierucci, J. Baima, B. Pamuk, J. Chaste, D. Utt, M. Bartos, K. Nogajewski, B. A. Piot, M. Orlita, M. Potemski, M. Calandra, M. C. Asensio, F. Mauri, C. Faugeras, A. Ouerghi, Flat electronic bands in long sequences of rhombohedral-stacked graphene. *Phys. Rev. B* **97**, 245421 (2018).
43. H. Zhou, T. Xie, A. Ghazaryan, T. Holder, J. R. Ehrets, E. M. Spanton, T. Taniguchi, K. Watanabe, E. Berg, M. Serbyn, A. F. Young, Half- and quarter-metals in rhombohedral trilayer graphene. *Nature* **598**, 429–433 (2021).
44. H. Zhou, T. Xie, T. Taniguchi, K. Watanabe, A. F. Young, Superconductivity in rhombohedral trilayer graphene. *Nature* **598**, 434–438 (2021).
45. A. Deshpande, W. Bao, F. Miao, C. N. Lau, B. J. LeRoy, Spatially resolved spectroscopy of monolayer graphene on SiO_2. *Phys. Rev. B* **79**, 205411 (2009).

46. C. Dutreix, M. I. Katsnelson, Friedel oscillations at the surfaces of rhombohedral *N*-layer graphene. *Phys. Rev. B* **93**, 035413 (2016).
47. R. Olsen, R. van Gelderen, C. M. Smith, Ferromagnetism in ABC-stacked trilayer graphene. *Phys. Rev. B* **87**, 115414 (2013).
48. C. Weeks, M. Franz, Interaction-driven instabilities of a dirac semimetal. *Phys. Rev. B* **81**, 085105 (2010).
49. B. Roy, I. F. Herbut, Unconventional superconductivity on honeycomb lattice: Theory of kekule order parameter. *Phys. Rev. B* **82**, 035429 (2010).
50. O. V. Gamayun, V. P. Ostroukh, N. V. Gnezdilov, İ. Adagideli, C. W. J. Beenakker, Valley-momentum locking in a graphene superlattice with y-shaped kekulé bond texture. *New J. Phys.* **20**, 023016 (2018).
51. A. L. Szabó, B. Roy, Metals, fractional metals, and superconductivity in rhombohedral trilayer graphene. *Phys. Rev. B* **105**, L081407 (2022).
52. U. Schollwöck, T. Jolicoeur, Haldane gap and hidden order in the S= 2 antiferromagnetic quantum spin chain. *EPL* **30**, 493–498 (1995).
53. F. Pollmann, E. Berg, A. M. Turner, M. Oshikawa, Symmetry protection of topological phases in one-dimensional quantum spin systems. *Phys. Rev. B* **85**, 075125 (2012).
54. G. E. Volovik, Flat band in topological matter. *J. Supercond. Novel Magn.* **26**, 2887–2890 (2013).
55. Y. Henni, H. P. Ojeda Collado, K. Nogajewski, M. R. Molas, G. Usaj, C. A. Balseiro, M. Orlita, M. Potemski, C. Faugeras, Rhombohedral multilayer graphene: A magneto-Raman scattering study. *Nano Lett.* **16**, 3710–3716 (2016).
56. J. M. Soler, E. Artacho, J. D. Gale, A. García, J. Junquera, P. Ordejón, D. Sánchez-Portal, The siesta method for ab initio order-*N* materials simulation. *J. Phys. Condens. Matter* **14**, 2745 (2002).
57. E. Artacho, E. Anglada, O. Diéguez, J. D. Gale, A. García, J. Junquera, R. M. Martin, P. Ordejón, J. M. Pruneda, D. Sánchez-Portal, J. M. Soler, The siesta method; developments and applicability. *J. Phys. Condens. Matter* **20**, 064208 (2008).
58. J. P. Perdew, K. Burke, M. Ernzerhof, Generalized gradient approximation made simple. *Phys. Rev. Lett.* **77**, 3865–3868 (1996).
59. H. J. Monkhorst, J. D. Pack, Special points for brillouin-zone integrations. *Phys. Rev. B* **13**, 5188–5192 (1976).
60. S. Dudarev, G. Botton, S. Savrasov, C. Humphreys, A. Sutton, Electron-energy-loss spectra and the structural stability of nickel oxide: An lsda+ u study. *Phys. Rev. B* **57**, 1505–1509 (1998).
61. C. Hubig, F. Lachenmaier, N.-O. Linden, T. Reinhard, L. Stenzel, A. Swoboda, M. Grundner, The SyTen toolkit. https://syten.eu/docs/index.html.
62. C. Hubig, "Symmetry-protected tensor networks," thesis, LMU München (2017).
63. C. Hubig, I. P. McCulloch, U. Schollwöck, F. A. Wolf, Strictly single-site dmrg algorithm with subspace expansion. *Phys. Rev. B* **91**, 155115 (2015).
64. I. P. McCulloch, From density-matrix renormalization group to matrix product states. *J. Stat. Mech. Theory Exp.* **2007**, P10014–P10014 (2007).
65. E. Stoudenmire, S. R. White, Studying two-dimensional systems with the density matrix renormalization group. *Annu. Rev. Condens. Matter Phys.* **3**, 111–128 (2012).
66. J. Ummethum, J. Schnack, A. M. Läuchli, Large-scale numerical investigations of the antiferromagnetic heisenberg icosidodecahedron. *J. Magn. Magn. Mater.* **327**, 103–109 (2013).
67. I. Hagymási, R. Schäfer, R. Moessner, D. J. Luitz, Possible inversion symmetry breaking in the *s* = 1/2 pyrochlore heisenberg magnet. *Phys. Rev. Lett.* **126**, 117204 (2021).
68. C. Hubig, J. Haegeman, U. Schollwöck, Error estimates for extrapolations with matrix-product states. *Phys. Rev. B* **97**, 045125 (2018).
69. S. Jung, G. M. Rutter, N. N. Klimov, D. B. Newell, I. Calizo, A. R. Hight-Walker, N. B. Zhitenev, J. A. Stroscio, Evolution of microscopic localization in graphene in a magnetic field from scattering resonances to quantum dots. *Nat. Phys.* **7**, 245–251 (2011).
70. S. Samaddar, I. Yudhistira, S. Adam, H. Courtois, C. B. Winkelmann, Charge puddles in graphene near the dirac point. *Phys. Rev. Lett.* **116**, 126804 (2016).
71. Y. Zhao, J. Wyrick, F. D. Natterer, J. F. Rodriguez-Nieva, C. Lewandowski, K. Watanabe, T. Taniguchi, L. S. Levitov, N. B. Zhitenev, J. A. Stroscio, Creating and probing electron whispering-gallery modes in graphene. *Science* **348**, 672–675 (2015).
72. J. Lee, D. Wong, J. Velasco Jr., J. F. Rodriguez-Nieva, S. Kahn, H.-Z. Tsai, T. Taniguchi, K. Watanabe, A. Zettl, F. Wang, L. S. Levitov, M. F. Crommie, Imaging electrostatically confined dirac fermions in graphene quantum dots. *Nat. Phys.* **12**, 1032–1036 (2016).
73. A. Weiße, G. Wellein, A. Alvermann, H. Fehske, The kernel polynomial method. *Rev. Mod. Phys.* **78**, 275–306 (2006).

Acknowledgments

Funding: The work was conducted within the framework of the Topology in Nanomaterials Lendulet project, grant no. LP2017-9/2/2017, with support from European H2020 GrapheneCore3 project no. 881603. L.T. acknowledges support from Elvonal grant KKP 138144. Z.T. acknowledges support from the UNKP-20-4 New National Excellence Program of the Ministry for Innovation and Technology through NKFIH. P.V. and L.O. acknowledge the support of the Janos Bolyai Research Scholarship and O.L. for the Bolyai+ Scholarship of the Hungarian Academy of Sciences. J.K. and L.O. acknowledge the support of Ministry of Innovation and Technology of Hungary within the Quantum Information National Laboratory. I.H. was supported, in part, by the Hungarian National Research, Development and Innovation Office (NKFIH) through grants no. K120569 and no. K134983. **Author contributions:** M.S.M.I., together with K.K., prepared and characterized the samples. STM measurements were performed by M.S.M.I., K.K., and P.N.-I. I.H. designed and performed the DMRG and mean-field calculations. Z.T. and P.V. provided the various tight-binding Hamiltonians. K.M., P.K., and A.P. were involved in the Raman spectroscopic mapping and sample preparation. Z.T. performed the ab initio calculations, under the supervision of J.K. with the assistance of P.V. L.O. and A.A. performed the tight-binding modeling of quantum confinement effects. L.T. contributed to data analysis. P.N.-I. conceived and coordinated the project and wrote the manuscript with input from all authors. **Competing interests:** The authors declare that they have no competing financial interests. **Data and materials availability:** All data needed to evaluate the conclusions in the paper are present in the paper and/or the Supplementary Materials. Data presented in the figures are available at https://doi.org/10.6084/m9.figshare.20318907.v1.

Submitted 20 February 2022
Accepted 20 July 2022
Published 2 September 2022
10.1126/sciadv.abo6879

ScienceAdvances

Observation of competing, correlated ground states in the flat band of rhombohedral graphite

Imre Hagymsi, Mohammad Syahid Mohd Isa, Zoltn Tajkov, Krisztin Mrity, Lszl Oroszlny, Jnos Koltai, Assem Alassaf, Pter Kun, Konrd Kandrai, Andrs Plinks, Pter Vancs, Levente Tapaszt, and Pter Nemes-Incze

Sci. Adv., **8** (35), eabo6879.
DOI: 10.1126/sciadv.abo6879

Science Advances (ISSN) is published by the American Association for the Advancement of Science. 1200 New York Avenue NW, Washington, DC 20005. The title *Science Advances* is a registered trademark of AAAS.